Supporting Data

Live-tracking of beef freshness at sub-ppb level ammonia detection with synergistic advancement in WS_2/rGO nanoflakes by edge site enriched acidic sulfur

Sonam Sonwal[a], Kugalur Shanmugam Ranjith[b], Subin Han[a], Young-Kyu Han[b,], Mi-Hwa Oh[c,*] Yun Suk Huh[a,*]*

[a]*NanoBio High-Tech Materials Research Center, Department of Biological Engineering, Inha University, Incheon 22212, Republic of Korea*

[b]*Department of Energy and Material Engineering, Dongguk University-Seoul, Seoul 04620, Republic of Korea*

[c]*National Institute of Animal Science, Rural Development Administration, Wanju 55365, Republic of Korea*

* Correspondence: yunsuk.huh@inha.ac.kr (Y.S.Huh), moh@korea.kr (M.-H.Oh), ykenergy@dongguk.edu (Y.-K.Han)

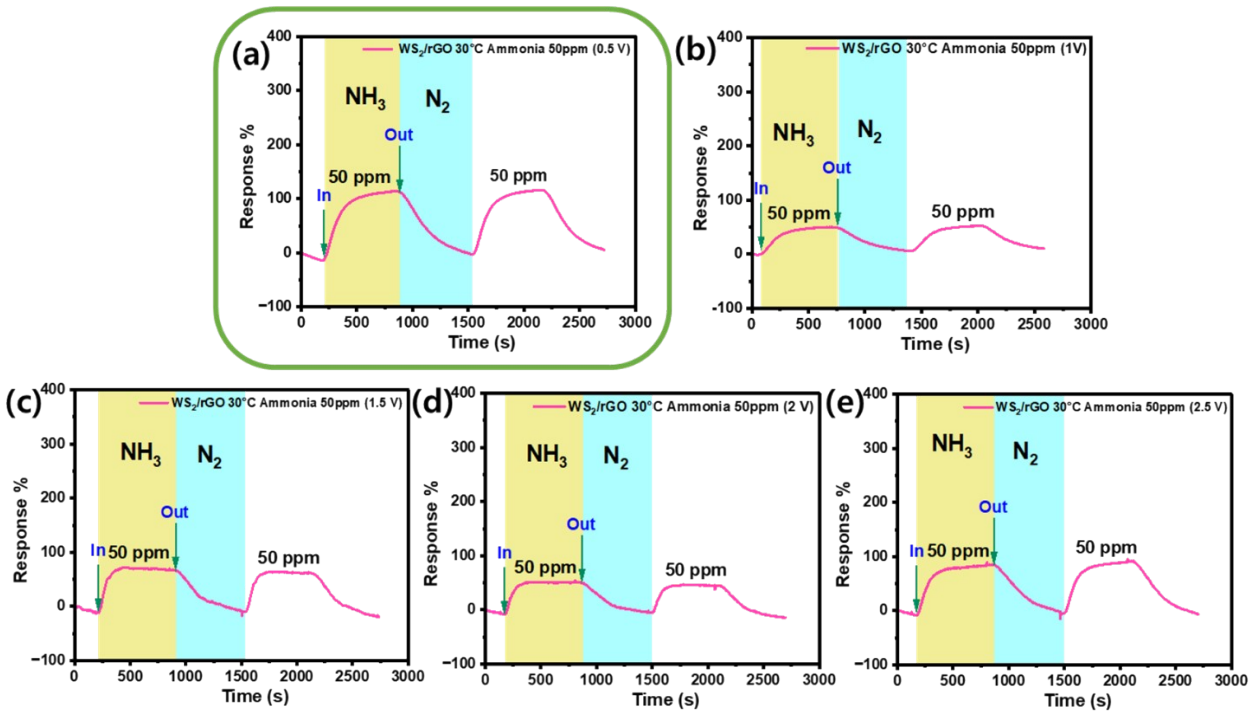

Fig. S1. Comparison of sensing performance of WS_2/rGO composite at different applied voltage. (a) 0.5V. (b) 1V. (c) 1.5V. (d) 2V. (e) 2.5V.

The sensor's response as functions of the provided bias voltage. At 0.5 V, the response rises to 120 (a), and at 2.5 V, it falls by 30 (e). The recovery also declines, going from 662 seconds at 0.5 V to 133 seconds at 1 V and finally to 377 seconds at 2.5 V. These findings are highly intriguing given that optimizing the applied voltage alone significantly improves sensing performance of the sensing electrode. Sensing response at 0.5 V showed the best response and recovery in comparison to the rest of the four volts, as represented in (a). Also, 0.5 V operating voltage supports our wireless device to be operated based on a coin cell.

The performance of a p-type semiconductor is significantly influenced by the exact location of the Fermi level. A crucial factor since it has a significant impact on the thermal, electrical, and, ultimately, functional characteristics of a semiconductor device. In p-type semiconductors, a closer Fermi level to the valence band results in more holes, which influence the behavior of the semiconductor as a whole because they are the majority carrier. A semiconductor is classified as p-type if its Fermi level is closer to the valence band and as n-type if it is closer to the conduction band. The application of an external voltage can alter this flow of holes or electrons, permitting the change in flow of current (positive or negative) and as applied voltage increases the conductivity decreases (hole-electron pair) and sensing response decreases. That said, the Fermi level positioning isn't static. The number of hole-electron pairs enhances, the Fermi level also moves towards the center of the bandgap, becoming intrinsic (less presence of electron in p-type semiconductors). The increase in intrinsic carriers alters the carrier distribution and thus affects the device's operation. As a result, in presence of ammonia additional electrons adsorbs on the surface having less holes (less conduction) leading to the accumulation of electrons over the surface or in other words less holes are available to interact with ammonia donated electrons, hence enhancing the conductivity of the material (high electron density, influencing the nature of p-type semiconductor) due to which at high voltage, low response resistance was observed.[1-4]

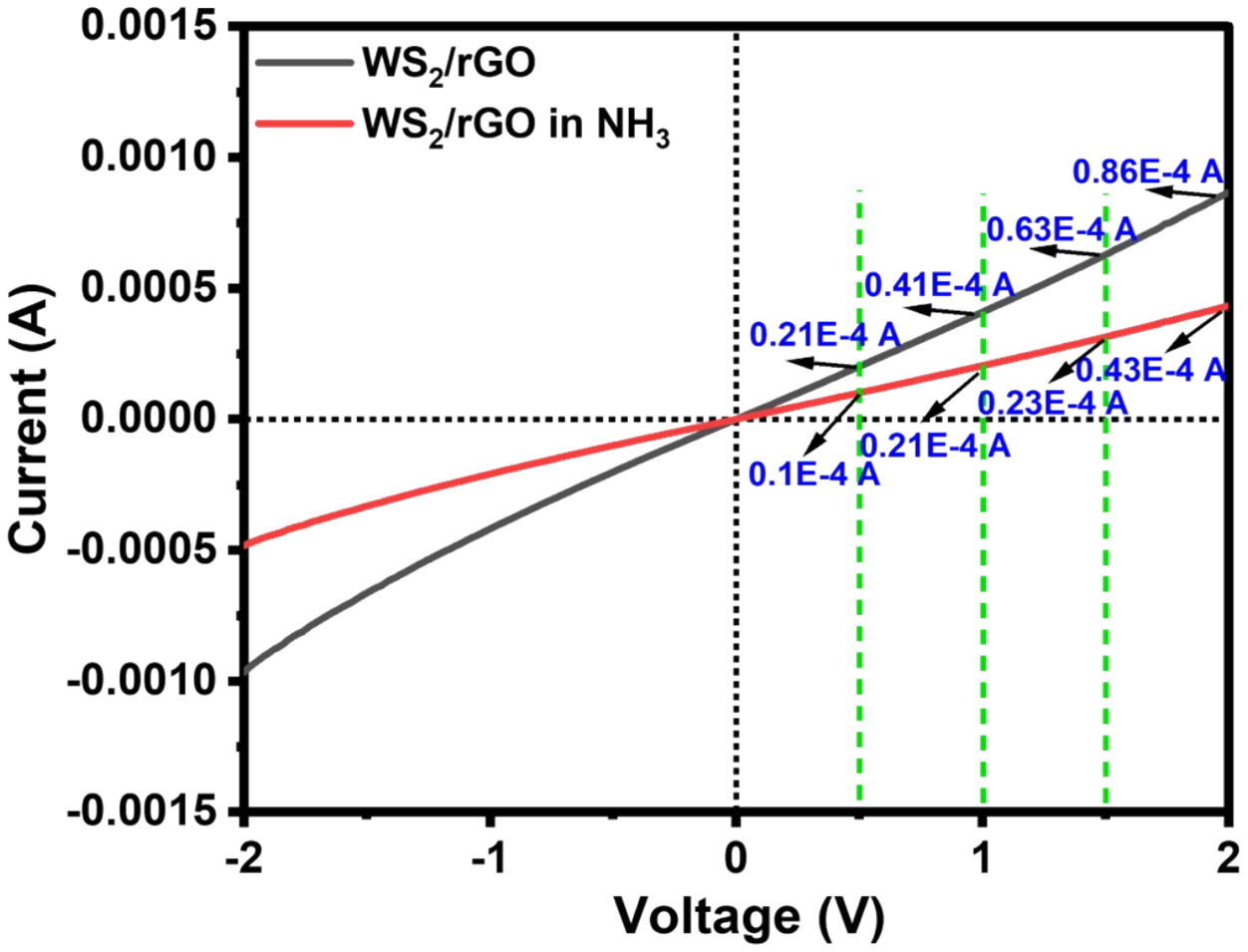

Fig. S2. I-V study for WS_2/rGO composite in presence and absence of NH_3.

I-V curve revealed that upon increasing voltage the current intensity also increased in presence of air and in presence of NH_3 same trend was observed but the current intensity is lower as compared to air environment. So, as the resistance is increasing it is supporting the sensing mechanism, for this reason we have chosen low voltage-high resistance parameter. Furthermore, our objective is to operate a commercial device so we have targeted low energy consumption which will be suitable for a coin cell-based device.

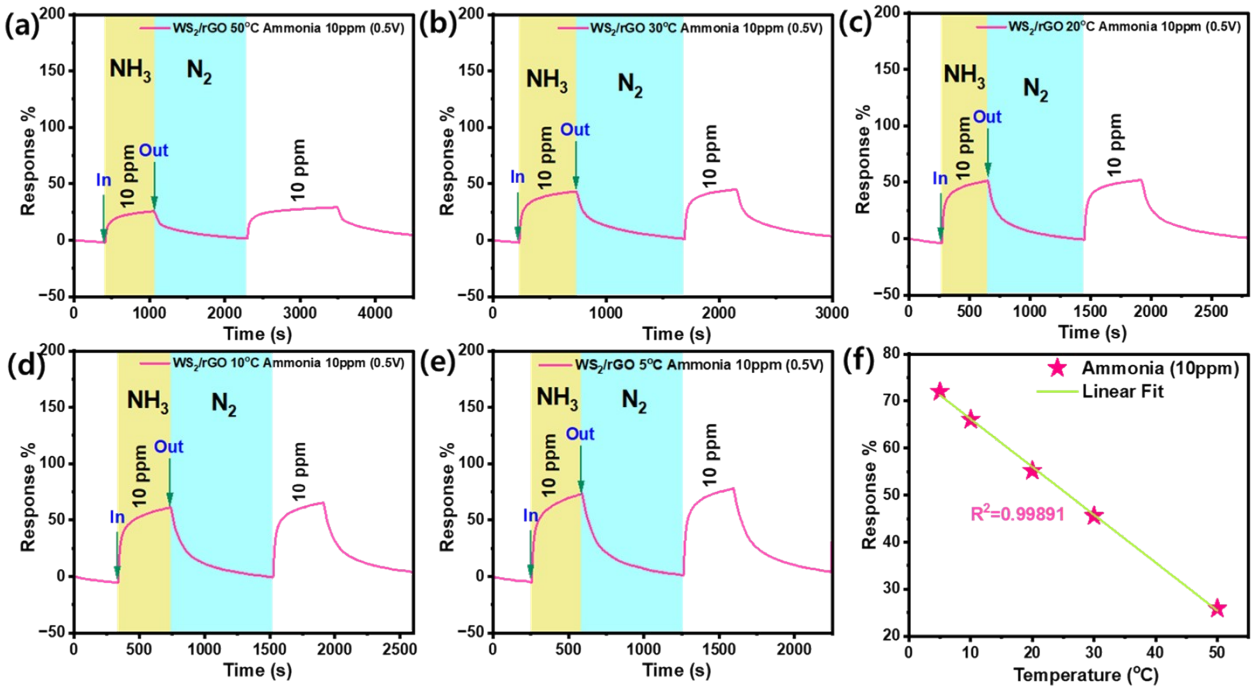

Fig. S3. Comparison of sensing performance of WS_2/rGO composite at different temperatures. (a) 50°C. (b) 30°C. (c) 20°C. (d) 10°C. (e) 5°C.

Temperature dependent study for the optimization of working temperature. Sensing response is inversely proportional to the temperature, on decreasing temperature the sensor showed more higher response. (b) According to the real-time monitoring target we operated all experiments at 30°C. (f) The relationship between temperature and response showed a linear trend with an R^2 value of 0.99891.

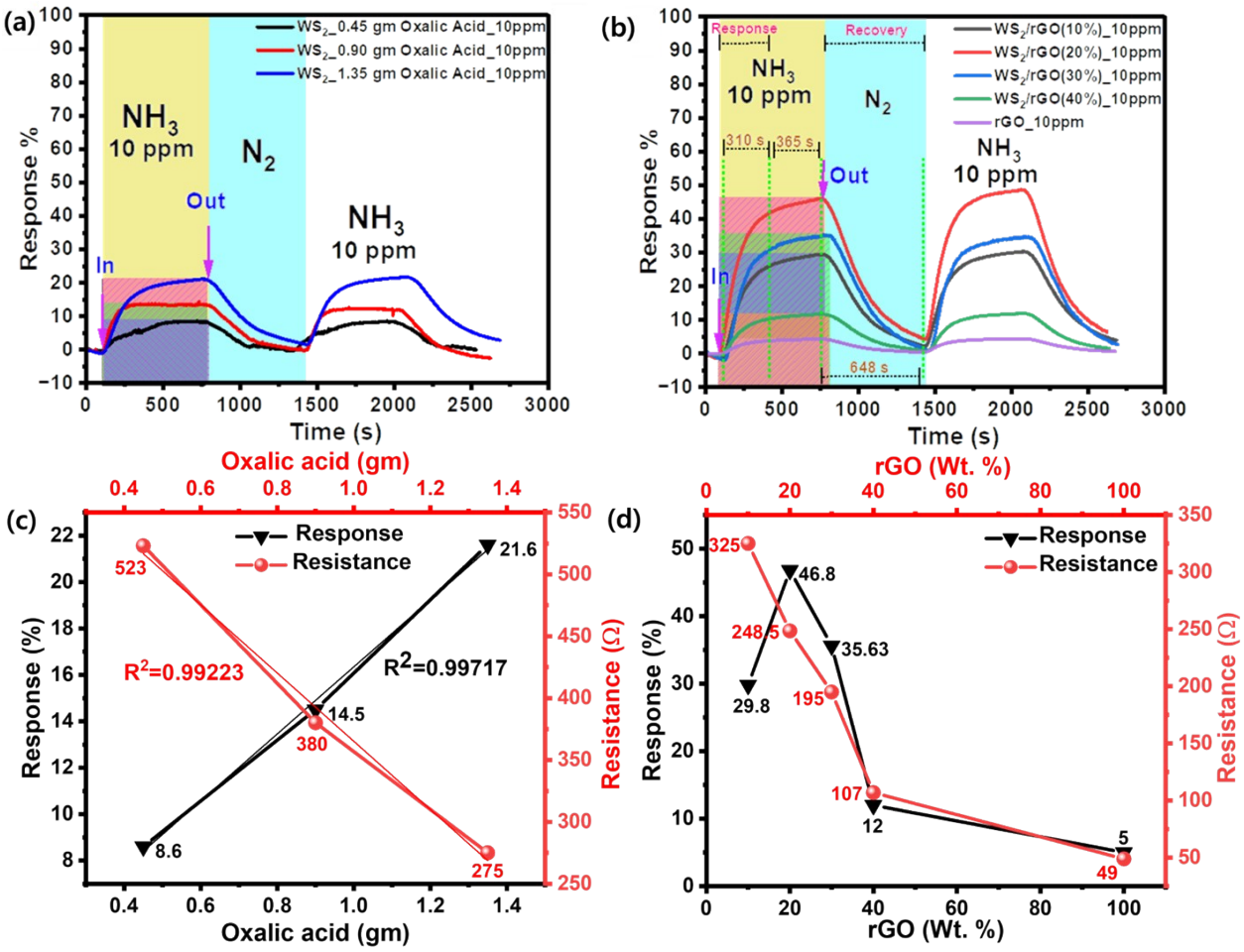

68

69 **Fig. S4.** Optimization of OA content and rGO content. (a) Sensing response comparison of WS_2
70 with different OA content. (b) Sensing response comparison of WS_2/rGO with different rGO
71 content. (c) Linear fit of sensing response and resistance of WS_2 with different OA content. (d)
72 linear fit for sensing response and resistance comparison of WS_2/rGO with different rGO content.
73

74 Oxalic acid content and rGO wt. % optimization for best performance of the sensor. (a and c)
75 Sensing response is proportional to the oxalic acid concentration, on increasing oxalic acid (1.35
76 gm) amount the sensor showed higher response, showed linear trend with R^2 vale of 0.99717. (b

77 and d) 20 wt. % of rGO compared to 100 wt. %, 10 wt. %, 30 wt. %, and 40 wt. %, showed highest

78 sensing response towards NH_3 at RT.

79

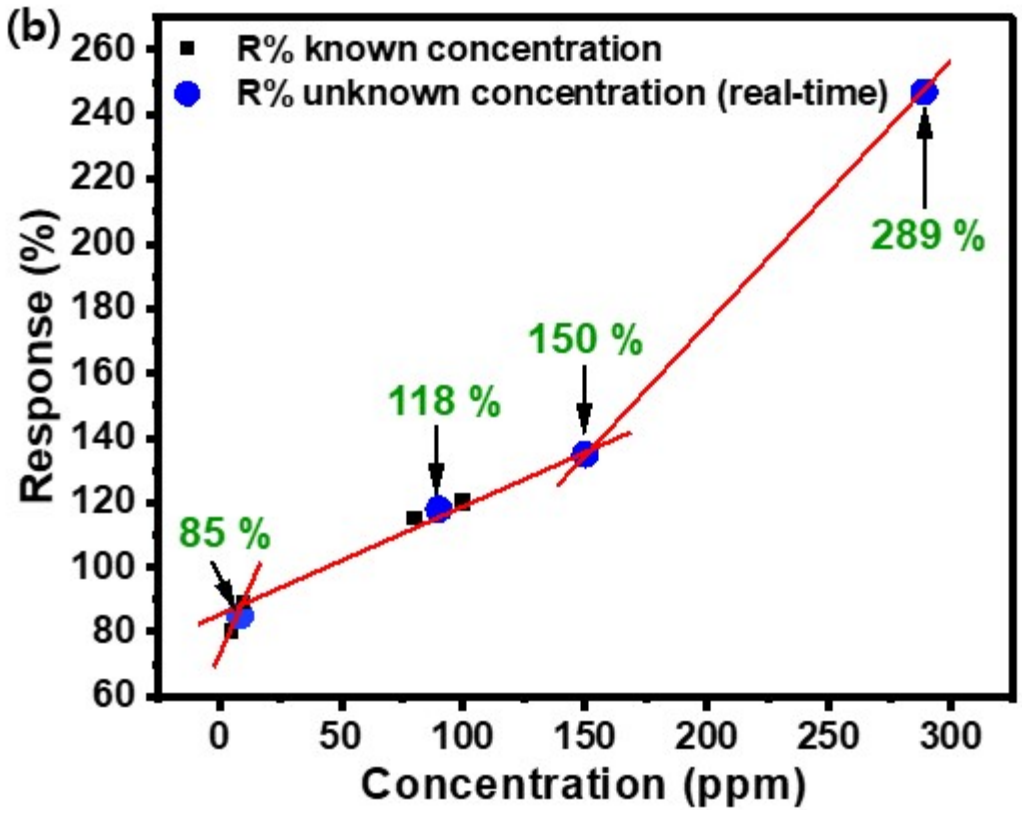

Fig. S5. Real-time monitoring sensor response % towards different concentration of NH_3 during meat spoilage. Comparison and calculation of unknown concentration of NH_3 during meat spoilage to set the admissible range for meat freshness. Below 150 response % meat is admissible to consume.

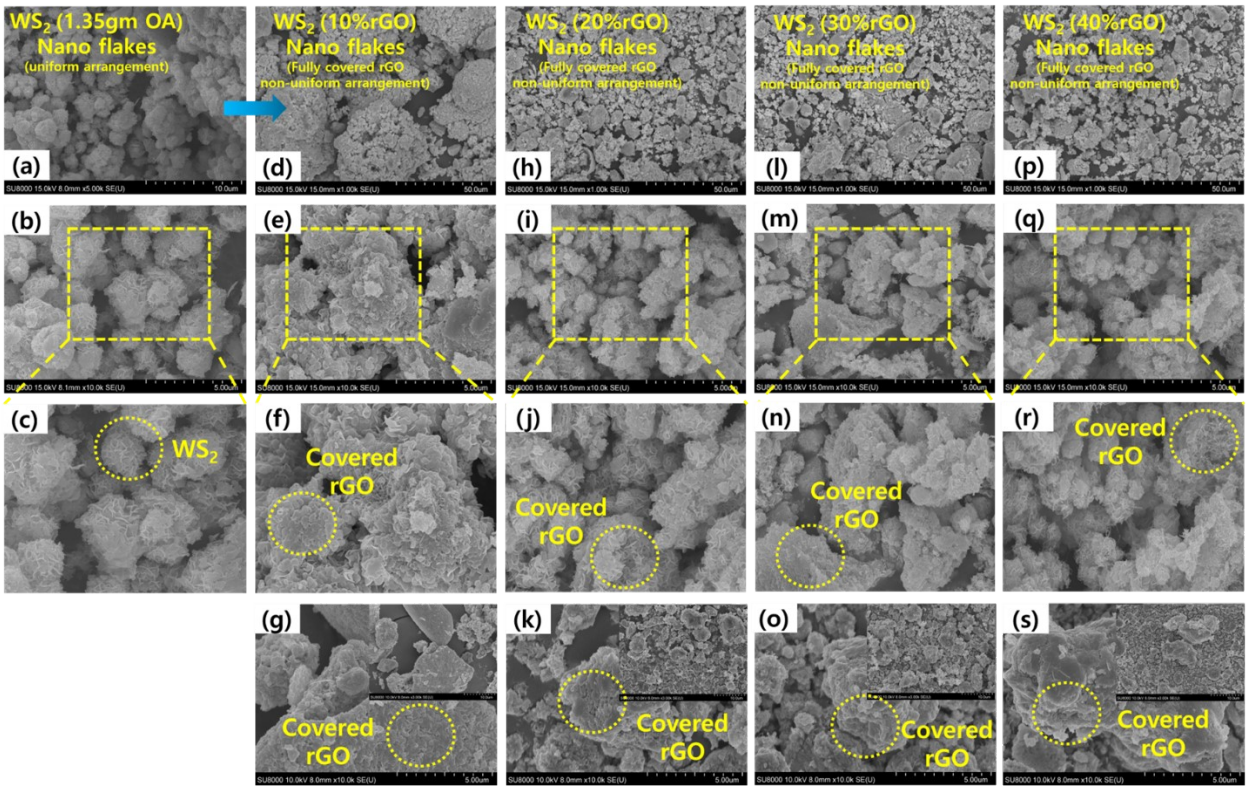

Fig. S6. HRSEM images of pristine WS_2 and all four composites at different magnifications to showcase the presence of rGO in all composites and their structural modifications. (a-c) WS_2. (d-g) WS_2 (10% rGO). (h-k) WS_2 (20% rGO). (l-o) WS_2 (30% rGO). (p-s) WS_2 (40% rGO).

HRSEM is used to examine the microstructure and morphology of all four composites. HRSEM images at various magnifications are shown in Fig. S6a-s. Synthesized sulfur-rich WS_2/rGO composites were primarily composed of nanoflakes (Fig. S6f,j,n, and r). High-magnification SEM (Fig. S6f,j,n, and r) revealed details of the microstructure of WS_2 nanoflakes and showed that they homogeneously and completely decorated rGO. Furthermore, the presence of rGO is shown in fig. S6g,k,o, and s, which represents that the morphology is disrupting over the addition of high rGO content (10%, 20%, 30%, and 40%) simultaneously maintaining the homogenous covering of all rGO particles.

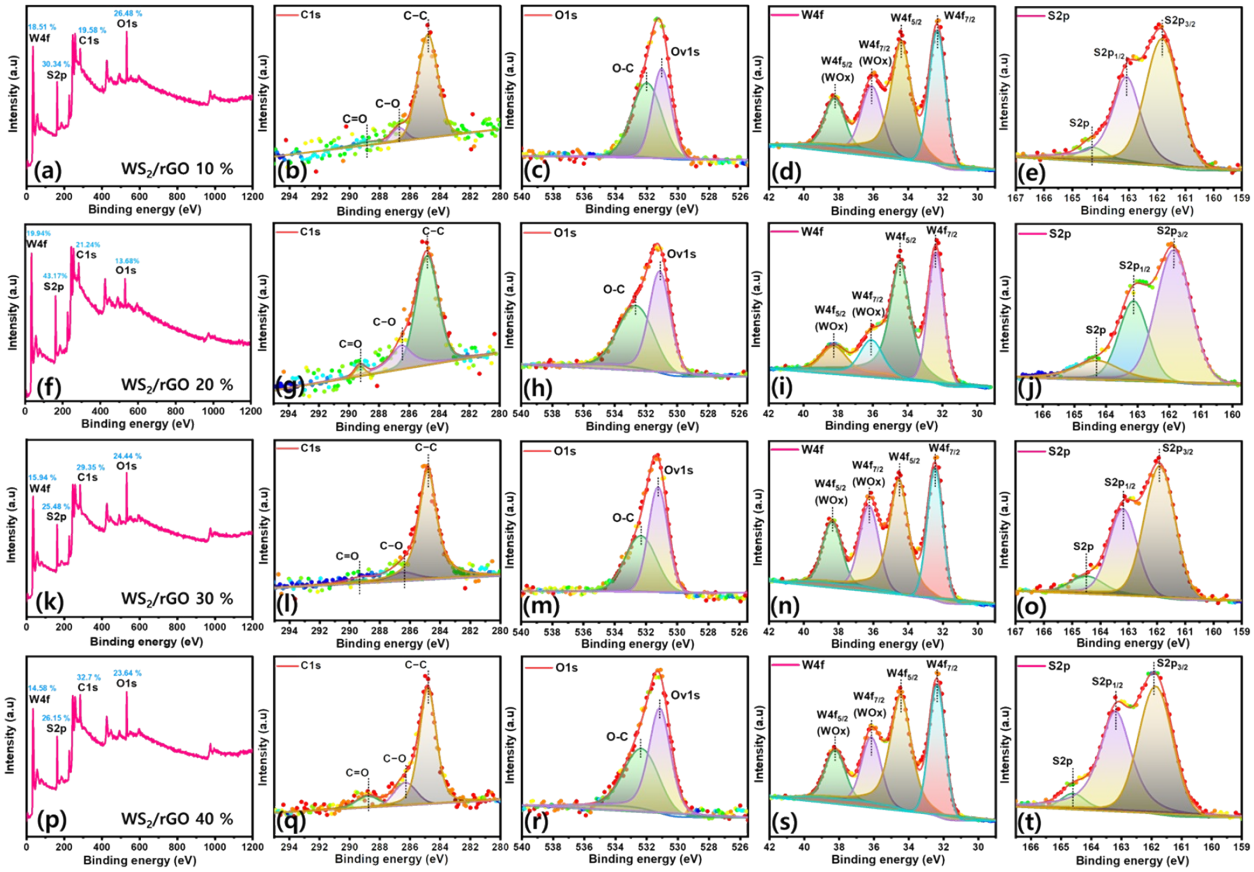

Fig. S7. XPS survey spectra of all four sulfur-rich WS_2/rGO composite; (a) WS_2 (10% rGO). (f) WS_2 (20% rGO). (k) WS_2 (30% rGO). (p) WS_2 (40% rGO) full scan survey spectra. (b-e) C1s, O1s, W4f, and S2p for WS_2 (10% rGO) composite. (g-j) C1s, O1s, W4f, and S2p for WS_2 (20% rGO) composite. (l-o) C1s, O1s, W4f, and S2p for WS_2 (30% rGO) composite. (q-t) C1s, O1s, W4f, and S2p for WS_2 (40% rGO) composite.

XPS analysis was performed to classify the molecular phases and oxidation states in all four different compositions of composites to evaluate the content ratio of all samples. The four core level peaks for W 4f, S 2p, C 1s, and O 1s are presented in (Fig. S7a,f,k and p) for all four samples (WS_2/rGO-10%, 20%, 30% and 40%), the percentage of carbon has increased with increase in

rGO content, the best performed composition with 20% rGO showed the least O_2 presence and highest W and S presence among all four compositions. The three core functional peaks at 284.8 eV (C-C), 286.4 eV (C-O), and 289.2 eV (C=O) represent C bonding (Fig. S7b,g,l, and q) and depict the C 1s deconvoluted spectrum of the sulfur-rich WS_2/rGO composites. Less intense O-bond signals in the C 1s spectrum of the composite further support its lower O-content. Observation of less O 1s state in the WS_2/rGO nanohybrids showed that the hydrothermal procedure effectively reduced GO to rGO. Fig. S7c,h,m, and r, shows the O 1s information, in which the main peak of O at 531.11 eV implies the existence of O-W bond in WS_2/rGO composites. In addition, a small peak at 532.65 eV is attributed to the sub-stoichiometric form of WS_2/rGO composites. The binding energies of two satellite shakeup peaks at 32.39 and 34.42 eV (Fig. 5d,i,n, and s) showed W $4f_{7/2}$ and W $4f_{5/2}$ are distinguishing features. Simultaneously, the modest peaks at 36.11 and 38.24 eV were attributed to W $4f_{7/2}$ and W $5p_{3/2}$ of oxides originating from WO_x and higher binding energies on the surface of the as-prepared sulfur-rich composites, notably 20% rGO ratio showed the least "O_2" presence with least intense peaks at 36.11 and 38.24 eV. Fig. S7e,j,o, and t, depicts the spectrum of S 2p, the binding energies of peaks at 161.86, 163.13 eV, and 164.29 eV denote divalent sulfide ions of S $2p_{3/2}$, S $2p_{1/2}$, and S 2p orbitals, respectively, used for W-S bonding. This shows the existence of unsaturated sulfur, and no S-O interaction peak was observed which supports the sensing mechanism or best performing composition (WS_2/rGO 20%). A possible site for humidity (RH) interaction. Two fundamental S $2p_{1/2}$ and S $2p_{3/2}$ peaks represent the common orbital states of S electrons. S has a valence of –2 in WS_2 and is represented by a pair of S $2p_{1/2}$ and S $2p_{3/2}$ peaks. Because of the possibility that the existence of sulfonated species ($–SO_3H$, the valence of S is +4) in the sulfur-rich WS_2/rGO

heterojunction, acid centers may inhibit. Thus, the peak of acid centers (SO_4^{2-}, the valence of S is +6) is absent in Fig. S7e,j,o, and t. A certain rise may be seen in the area ratio between $S2p_{1/2}$ and $S2p_{3/2}$, which indicates an increase in S^{4+} content. With a +4 valence of the S element, it represents the existence of sulfonated species $–SO_3H$ and sulfur richness of the composite material.

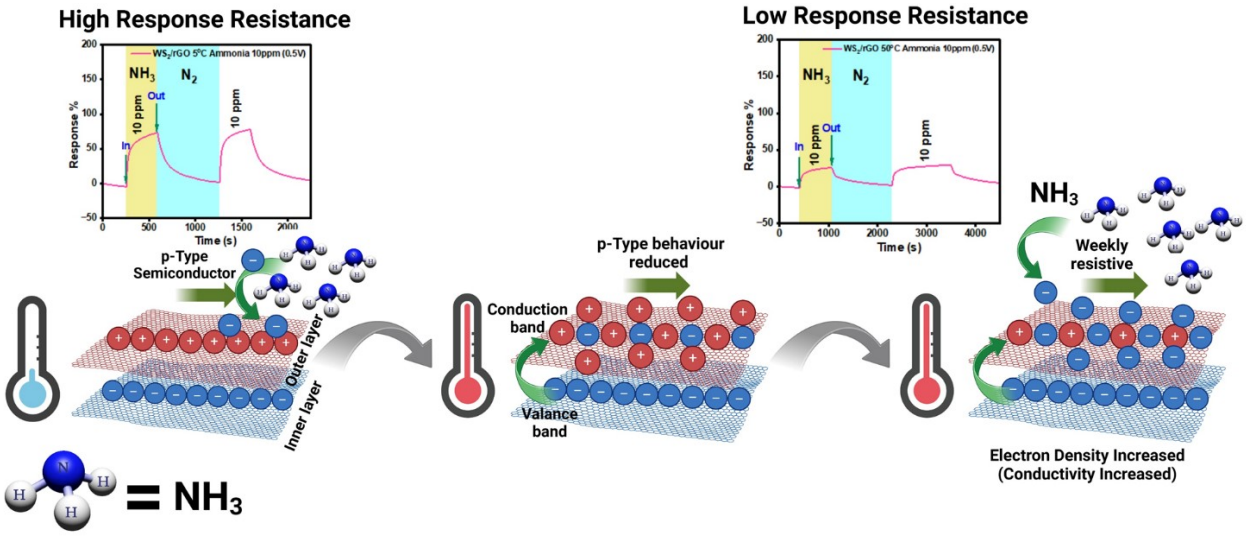

Fig. S8. Schematic presentation of sensing mechanism at low and high temperature.

In P-type semiconductors, the conductivity (flow of positive charge) decreases with increasing temperature due to the decrease in number of holes. At low temperatures, the holes are highly concentrated and act as majority charge carriers, while at the higher temperatures, thermal energy promotes some of the holes to the valance band, reducing the number of available holes for conduction or the intrinsic charge carrier concentration (i.e., electron-hole pair) also increases. With more pairs, holes can recombine with electrons, reducing the rate of hole flow, and consequently, the conductivity drops. Simultaneously, in presence of ammonia additional electrons adsorbs on the surface having less holes (less conduction) leading to the accumulation of electrons over the surface or in other words less holes are available to interact with ammonia donated electrons, hence enhancing the conductivity of the material (high electron density, influencing the nature of semiconductor) due to which at high temperature, low response resistance was observed. This behavior can be explained by the band theory of solids. In semiconductors, the

valence band and conduction band are separated by a band gap, which determines the energy required for an electron to move from the valence band to the conduction band and become a free electron. At low temperatures, the electrons are mostly in the valence band, and few are able to overcome the energy barrier and enter the conduction band (nature of p-type semiconductors). However, as the temperature increases, more electrons are able to gain enough thermal energy to move into the conduction band, increasing the conductivity.[4-7]

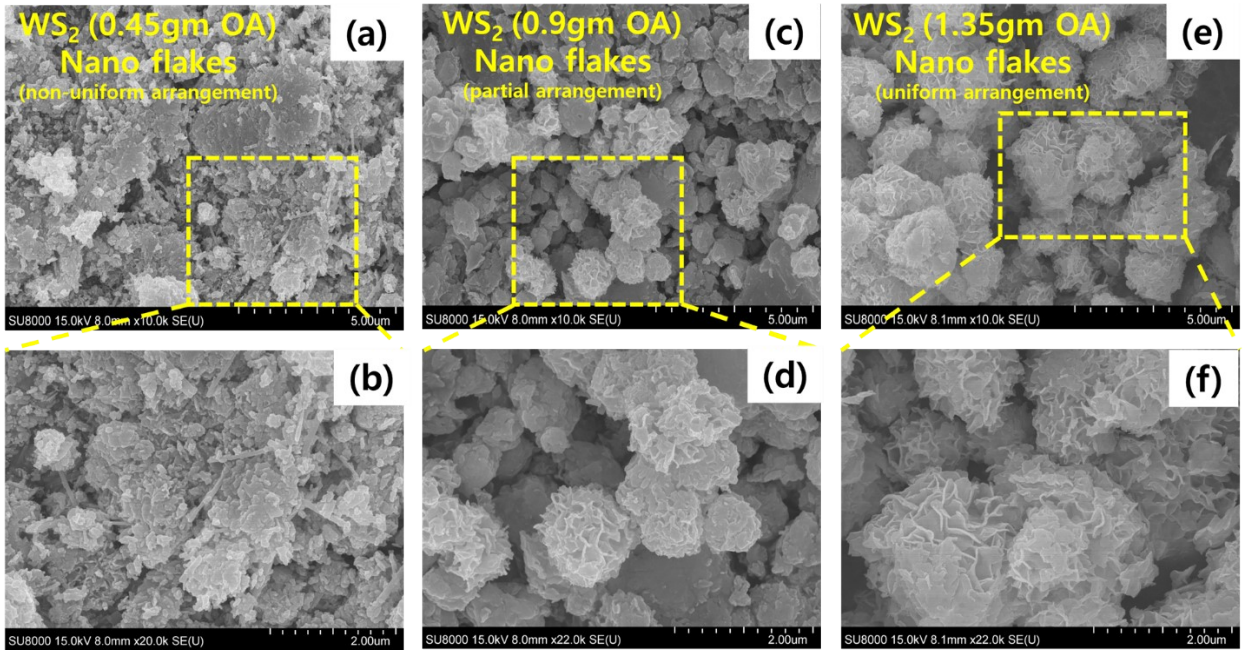

158

159 **Fig. S9.** HRSEM images of WS_2 with different OA content at different resolutions. (a, b) WS_2

160 (0.45 gm OA). (c, d) WS_2 (0.45 gm OA). (e,f) WS_2 (0.45 gm OA).

161

162 HRSEM is used to examine the microstructure and morphology of all three pristine WS_2

163 nanomaterials (Fig. S9a,c, and e). HRSEM images at high magnifications are shown in Fig. S9b,d,

164 and f. Synthesized sulfur-rich WS_2 nanomaterials were primarily composed of nanoflakes. High-

165 magnification of all three samples revealed details of the microstructure of WS_2 nanoflakes and

166 showed that on increasing oxalic acid (OA) content the best performed pristine nanomaterial (WS_2,

167 1.35 gm OA) showed the perfect microstructure with homogenous formation of nanoflakes.

168

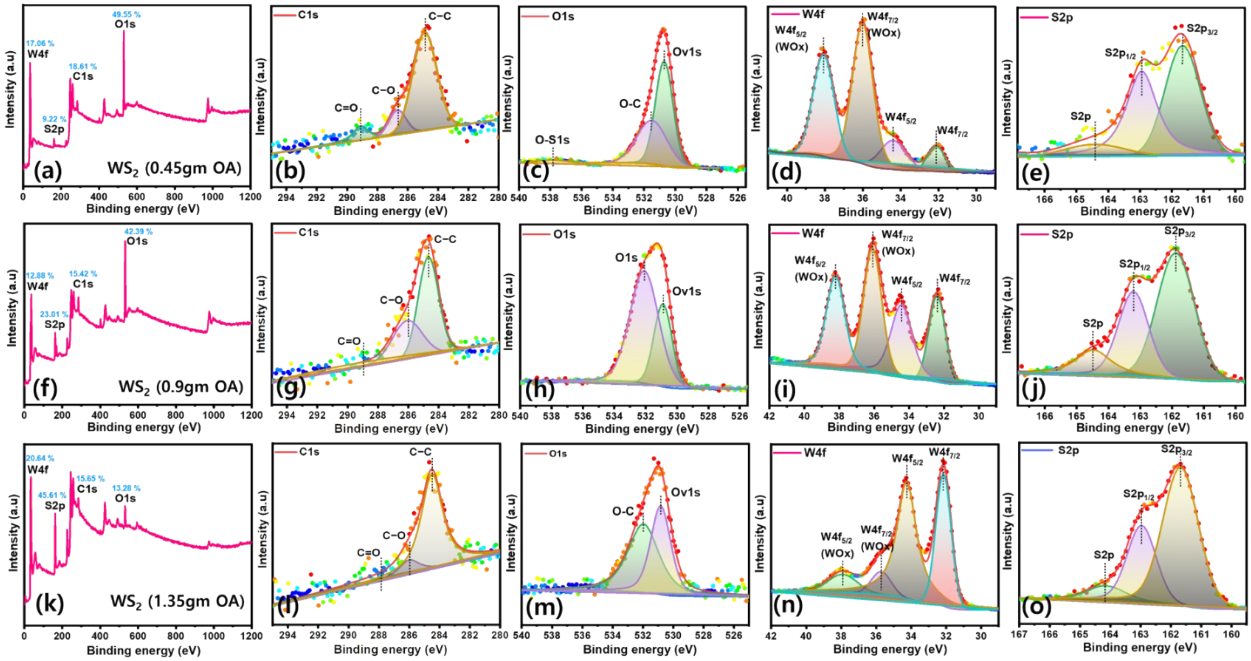

169

170 **Fig. S10.** XPS survey spectra of all three pristine WS_2 with different OA content; (a) WS_2 (0.45
171 gm OA). (f) WS_2 (0.90 gm OA). (k) WS_2 (1.35 gm OA). full scan survey spectra. (b-e) C1s, O1s,
172 W4f, and S2p for WS_2 (0.45 gm OA). (g-j) C1s, O1s, W4f, and S2p for WS_2 (0.90 gm OA). (l-o)
173 C1s, O1s, W4f, and S2p for WS_2 (1.35 gm OA).

174

175 XPS analysis was performed to classify the molecular phases and oxidation states in all three
176 pristine WS_2 samples to evaluate the effect of OA. The four core level peaks for W 4f, S 2p, C 1s,
177 and O 1s are presented in (Fig. S10a,f, and k) for all three samples (WS_2 with 0.45, 0.9, and 1.35
178 gm OA). The best performed pristine nanomaterial (WS_2 with 1.35 gm OA) showed the sulfur
179 richness and highest intensities of W4f peaks at the binding energies of two satellite shakeup peaks
180 at 32.39 and 34.42 eV (Fig. S10n) showed W $4f_{7/2}$ and W $4f_{5/2}$ are distinguishing features.
181 Simultaneously, the modest peaks at 36.11 and 38.24 eV were attributed to W $4f_{7/2}$ and W $5p_{3/2}$ of
182 oxides originating from WO_x which are least intense compared to less content of OA samples.

Notably presence of 1.35gm OA showed the least "O_2" presence with least intense peaks at 36.11 and 38.24 eV (Fig. S10k). Fig. S10e,j, and o, depicts the spectrum of S 2p, the binding energies of peaks at 161.86, 163.13 eV, and 164.29 eV denote divalent sulfide ions of S $2p_{3/2}$, S $2p_{1/2}$, and S 2p orbitals, respectively, used for W-S bonding. This shows the existence of unsaturated sulfur. Two fundamental S $2p_{1/2}$ and S $2p_{3/2}$ peaks represent the common orbital states of S electrons. S has a valence of –2 in WS_2 and is represented by a pair of S $2p_{1/2}$ and S $2p_{3/2}$ peaks. Because of the possibility that the existence of sulfonated species ($–SO_3H$, the valence of S is +4) in the sulfur-rich WS_2 heterojunction, acid centers may inhibit. Thus, the peak of acid centers ($SO_4^{2–}$, the valence of S is +6) is absent in Fig. S7e,j, and o. A certain rise may be seen in the area ratio between $S2p_{1/2}$ and $S2p_{3/2}$, which indicates an increase in S^{4+} content. With a +4 valence of the S element, it represents the existence of sulfonated species $–SO_3H$ and sulfur richness of the composite material.

196 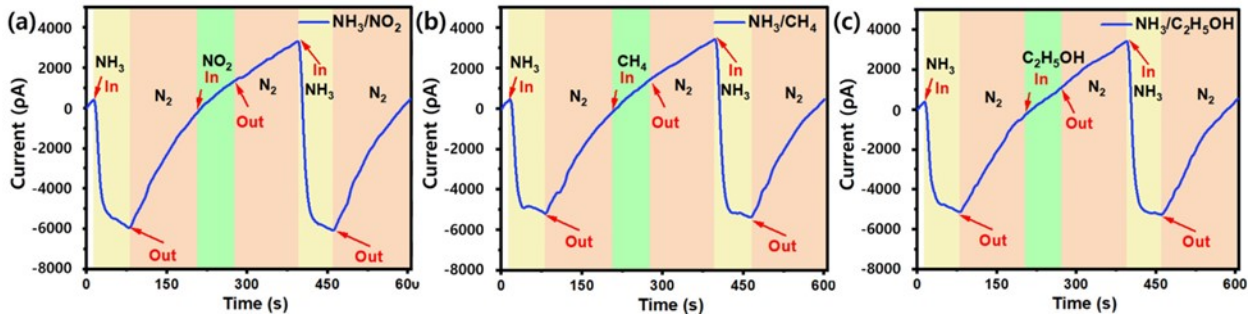

197 **Fig. S11a.** Cross reactivity analysis for BLE device integrated with fabricated sensor for different

198 gases (separately). (a) NO_2. (b) CH_4. (c) C_2H_5OH.

199 In presence of NO_2, CH_4, C_2H_5OH (Fig. S11a: a, b, c, respectively) gases no interference was

200 observed, which proves that sulfur-rich WS_2/rGO nanohybrid is highly specific towards NH_3 gas.

201

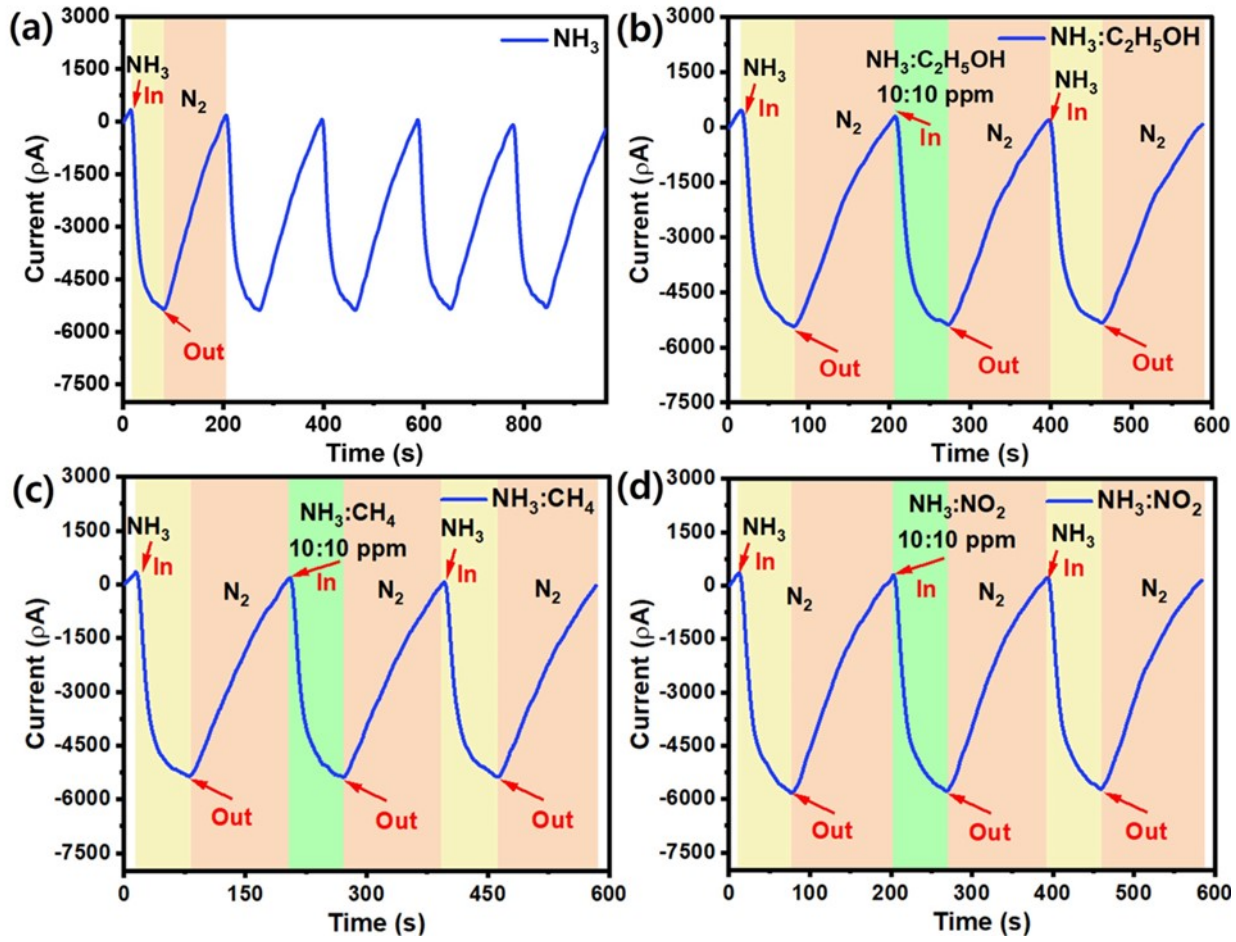

202

203 **Fig. S11b.** Cross reactivity analysis for BLE device integrated with fabricated sensor for different

204 gases (mixture). (a) NH_3. (b) NH_3:C_2H_5OH. (c) NH_3:CH_4. (d) NH_3:NO_2.

205 In presence of NH_3:NO_2, NH_3:CH_4, NH_3:C_2H_5OH (Fig. S11b: a, b, c, d, respectively) mixture of

206 gases no interference was observed, which again proves that sulfur-rich WS_2/rGO nanohybrid is

207 highly specific towards NH_3 gas (Video S1).

208

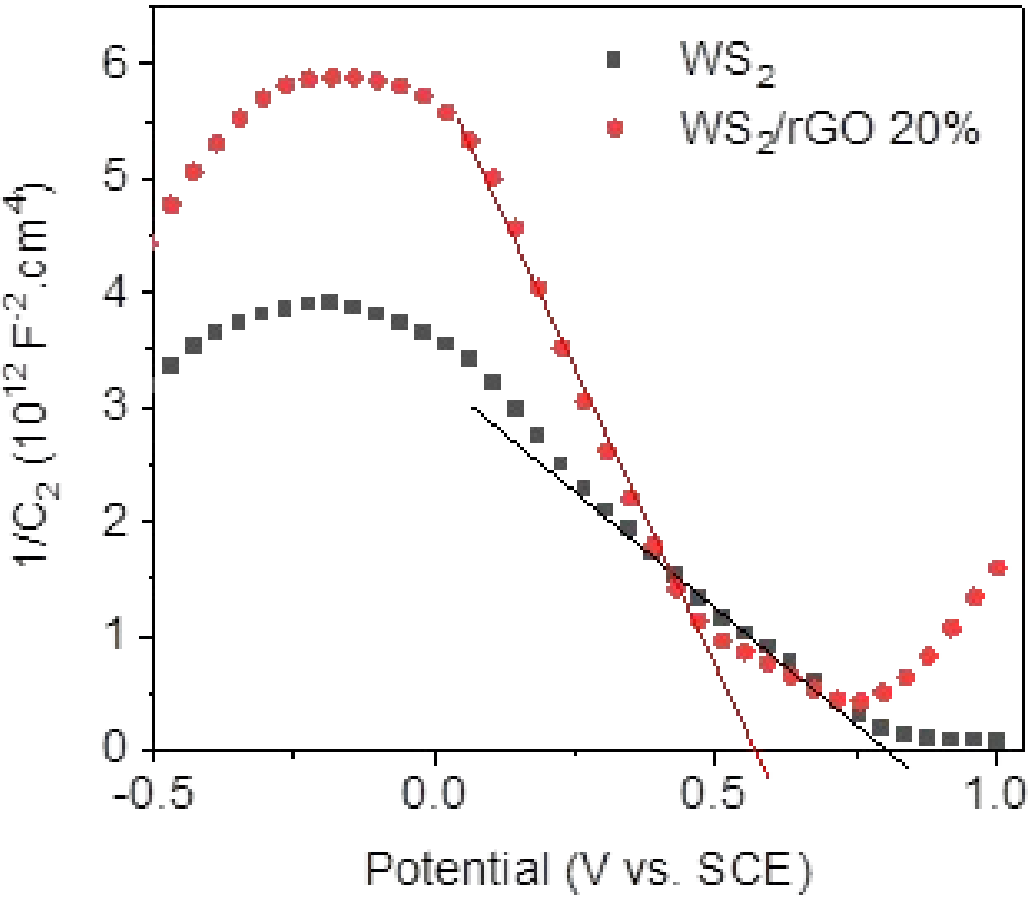

209

210 **Fig. S12.** Mott Schottky plot for all three samples rGO, WS_2, WS_2/rGO.

211 M-S plot showed the p-type behavior of the semiconductor. Sulfur richness and nitrogen
212 environment played a crucial role in making WS_2 and rGO as a p-type semiconductor as S and N
213 acted as acceptor and supported (enhanced) the interaction of NH_3 electrons.

214

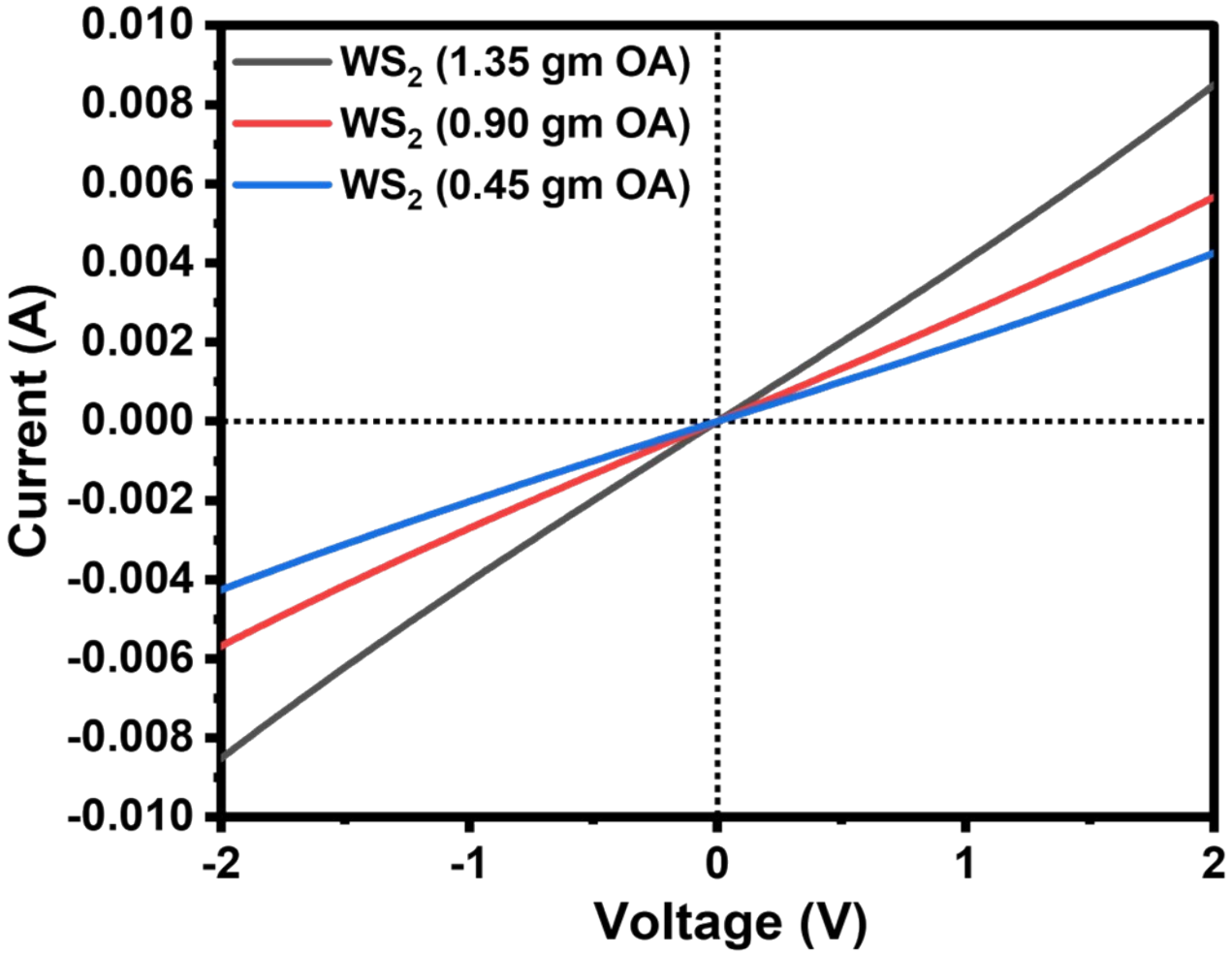

215

216 **Fig. S13.** I-V study for WS_2 with different OA content.

217

Table S1. Ammonia ppm calculation for real time monitoring of meat freshness

Standard concentration		Real-time monitoring		
PPM	**R%**	**R%**	**PPM**	**Admissible**
5	80	85	8.4	o
10	89	118	90	o
80	115	135	150	x
100	120	247	289	x

Table S2. rGO content calculation for all four composites

Content of rGO in WS_2/rGO nanohybrid					
rGO (40ml GO solution)	WS_2 (40ml solution)	WS_2/rGO 10% (40ml solution)	WS_2/rGO 20% (40ml solution)	WS_2/rGO 30% (40ml solution)	WS_2/rGO 40% (40ml solution)
250 mg	350 mg	62.5/350 Ratio: 18	125/350 Ratio: 35	187.5/350 Ratio: 53	250/350 Ratio: 71
XPS analysis for rGO content in WS_2/rGO nanohybrid					
85.91 %	17.65 %	19.52-17.65 % = 1.87 %	24.24-17.65 % = 6.59 %	29.35-17.65 % = 11.7 %	32.7-17.65 % = 15.05 %

Table S3: Comparison of C, O, W, and S atomic % in all composites

Composite	C %	O %	W %	S %
WS_2/rGO 10%	19.58	26.48	18.51	30.34
WS_2/rGO 20%	21.24	13.68	19.94	43.17
WS_2/rGO 30%	29.35	24.44	15.94	25.48
WS_2/rGO 40%	32.7	23.64	14.58	26.15

Video S1: Working demonstration of BLE sensing device for NH_3:C_2H_5OH mixture in same cycles.

References

1 K. Choi, G. Jung, S. Hong, Y. Jeong, W. Shin, J. Park, C. Lee, D. Kim and J. H. Lee, *Int. Symp. Olfaction Electron. Nose, ISOEN 2022 - Proc.*, 2022, 1–4.

2 Y. Kim, T. Kim, Y. S. Choi, T. H. Lee, H. Park, S. A. Lee, H. G. Byun, B. H. Hong and H. W. Jang, *Sensors Actuators B Chem.*, 2021, 349.

3 Q. Feng, X. Li, J. Wang and A. M. Gaskov, *Sensors Actuators, B Chem.*, 2016, **222**, 864–870.

4 Y. C. Wang, *Introduction to the Semiconductor Process Technologies*, 2004.

5 Why Does Conductivity Increase With Temperature In Semiconductors?, https://atlas-scientific.com/blog/why-does-conductivity-increase-with-temperature-in-semiconductors/.

6 G. S. Nolas and H. J. Goldsmid, *Therm. Conduct.*, 2006, 105–121.

7 D. Radisky, M. J. Bissell, K. Illmensee, M. J. Bissell, S. A. Ravani, M. J. Blaser, M. A. Peppercorn, B. Vogelstein and C. Eng, *Thermoelectricity in*, 2004, vol. 303.